JACS
JOURNAL OF THE AMERICAN CHEMICAL SOCIETY
pubs.acs.org/JACS
Article

Superconductivity in Layered van der Waals Hydrogenated Germanene at High Pressure

Yilian Xi,◆ Xiaoling Jing,◆ Zhongfei Xu,◆ Nana Liu, Yani Liu, Miao-Ling Lin, Ming Yang, Ying Sun, Jincheng Zhuang, Xun Xu, Weichang Hao, Yanchun Li, Xiaodong Li, Xiangjun Wei, Ping-Heng Tan, Quanjun Li,* Bingbing Liu,* Shi Xue Dou, and Yi Du*

Cite This: J. Am. Chem. Soc. 2022, 144, 18887−18895

ABSTRACT: The emergence of superconductivity in two-dimensional (2D) materials has attracted tremendous research efforts because the origins and mechanisms behind the unexpected and fascinating superconducting phenomena remain unclear. In particular, the superconductivity can survive in 2D systems even with weakened disorder and broken spatial inversion symmetry. Here, structural and superconducting transitions of 2D van der Waals (vdW) hydrogenated germanene (GeH) are observed under compression and decompression processes. GeH possesses a superconducting transition with a critical temperature (T_c) of 5.41 K at 8.39 GPa. A crystalline to amorphous transition occurs at 16.80 GPa, while superconductivity remains. An abnormal increase of T_c up to 6.11 K was observed during the decompression process, while the GeH remained in the 2D amorphous phase. A combination study of *in situ* high-pressure synchrotron X-ray diffraction, *in situ* high-pressure Raman spectroscopy, transition electron microscopy, and density functional theory simulations suggests that the superconductivity in 2D vdW GeH is attributed to the increased density of states at the Fermi level as well as the enhanced electron−phonon coupling effect under high pressure even in the form of an amorphous phase. The unique pressure-induced phase transition of GeH from 2D crystalline to 2D amorphous metal hydride provides a promising platform to study the mechanisms of amorphous hydride superconductivity.

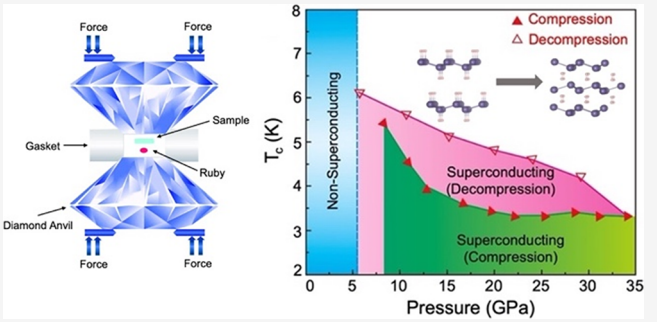

INTRODUCTION

Single or few-layer two-dimensional (2D) van der Waals (vdW) materials are not expected to exhibit correlated ground states such as superconductivity. This is because their vanishingly small Fermi surface or sizeable energy gap at the Fermi level dramatically suppresses electron−electron interactions even at low temperatures.[1−3] In addition, thin layered 2D vdW materials possess quite weak electron−phonon coupling (EPC) because of thermal fluctuations, which consequently suppresses the formation of cooper pairs. The emergence of superconductivity in 2D vdW materials is, therefore, always significant for exploring the mechanism of strong electronic correlations in low-dimension systems. A number of previous works have proven that the superconductivity can be evoked in 2D vdW materials by increasing electron density at the Fermi level and enhancing EPC. For example, gating of monolayer WTe_2 was proven to induce a topological phase transition from a trivial band insulator to a superconductor with significantly increased charge carrier density.[4] A phonon-mediated superconductivity in graphene can be achieved by doping alkali adatoms at honeycomb hole positions, which gives rise to enhanced EPC and electron density.[5−9] Recent advances in "magic-angle" graphene demonstrate that the strongly correlated phase can be triggered in twisted bilayer graphene with enhanced interlayer interaction, in which two van Hove singularities line up with the Fermi level and result in a high density of states (DOS) at the Fermi level accompanied by unconventional superconductivity.[10] Although such exciting superconductivity was observed in 2D vdW materials, it remains extremely challenging to realize strongly correlated phenomena, such as superconductivity, in 2D vdW materials with weak interlayer interaction and in disordered structures.

Germanene, a germanium-based layered 2D vdW material in a low-buckled honeycomb lattice, possesses Dirac electronic states in the low-energy region.[11−18] Topological insulating states and the quantum spin Hall effect are expected to emerge in this 2D material.[19,20] However, its mixed sp^2/sp^3 hybridization states lead to a structural instability that consequently

Received: May 29, 2022
Published: October 4, 2022

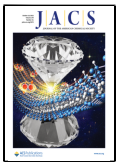

https://doi.org/10.1021/jacs.2c05683
J. Am. Chem. Soc. 2022, 144, 18887−18895

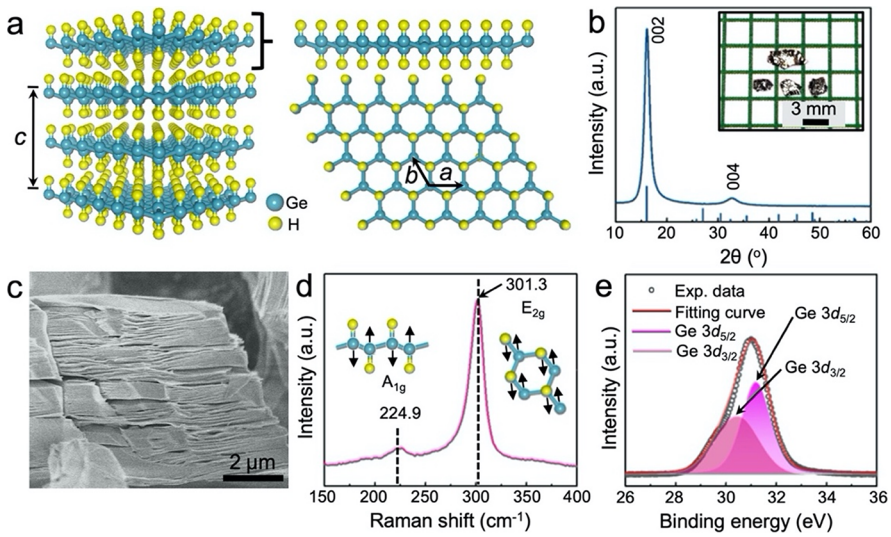

Figure 1. Structural characterization of 2H GeH at ambient pressure. (a) The crystal structure of the 2D vdW layered GeH. The blue and yellow balls represent the Ge and H atoms, respectively. (b) Powder XRD pattern of the GeH single crystal (inset: image of GeH single crystals). (c) SEM image of GeH indicates its layered structure. (d) Raman spectrum of GeH product. The insets show phonon modes of GeH, where E_{2g} represents Ge−Ge in-plane vibration and A_{1g} represents Ge−H out-of-plane vibration. (e) The XPS spectrum of Ge 3d in the GeH sample.

suppresses its exotic properties.[21] Recently, hydrogenated germanene (GeH) has been successfully synthesized, in which the structure of germanene is stabilized by hydrogen atoms terminated on top of Ge sites.[22−29] The hydrogen atoms covalently bond on both sides of the germanene, which not only form an ordered hexagonal hydrogen sublattice but also open a direct band gap of 1.5 eV in GeH. It should be noted that superconductivity can be induced in 2D Dirac materials in a honeycomb lattice through chemical decoration if the adatoms form an ordered structure.[5−9] Although GeH meets such criteria, its semiconducting nature leads to zero DOS at the Fermi level, and no superconductivity has ever been observed in GeH as yet.

Here, we report a pressure-induced superconductivity in a 2D vdW layered GeH single crystal. The pressure-driven transition from a semiconducting state to a superconducting state occurs at 8.39 GPa with a superconducting critical temperature (T_c) of 5.41 K. An abnormal increase of T_c to 6.11 K has been observed in the decompression process. Experimental characterizations reveal that the superconducting GeH undergoes an irreversible phase transition from a 2D crystalline to 2D amorphous phase upon the high pressure applied. Together with theoretical simulation, we find that the emergence of superconducting transition in compressed GeH is mainly due to the enhancement of the DOS at the Fermi level and the EPC under high pressure, while the abnormal increase of T_c during decompression is attributed to the softening of the in-plane Ge−Ge phonon mode. The mechanism of this rare 2D amorphous superconductivity was also explored. This work not only develops a strategy of creating superconductivity in 2D vdW layered hydrides but also promotes the understanding of superconductivity in 2D amorphous compounds.

RESULTS AND DISCUSSION

GeH exhibits a typical 2D vdW layered structure, in which the low-buckled Ge plane in each layer is saturated by H atoms on the surface,[22−24] as illustrated in Figure 1a. GeH single crystal samples in the size of several millimeters were prepared by a topochemical deintercalation method (Figure 1b inset). The structure of the synthesized GeH sample is characterized by X-ray diffraction (XRD). As shown in Figure 1b, all peaks of the GeH single crystal can be well indexed to a 2H phase in the space group $P63/mc$ (see XRD of GeH powder in Figure S1). The 2D layered structure of GeH crystal is demonstrated by the scanning electron microscopy (SEM), as shown in Figure 1c. Elemental mapping was also performed by energy dispersive X-ray spectroscopy (EDS) to investigate the elemental dispersion. As displayed in Figure S2, the Ge element is uniformly distributed on the GeH surface. The Raman spectrum of the GeH sample in Figure 1d shows two phonon peaks at 301.27 and 224.85 cm^{-1}, which are assigned to the in-plane E_{2g} and the out-of-plane A_{1g} vibrational modes, respectively.[22] The X-ray photoelectron spectroscopy (XPS) spectrum of the sample shows two peaks at binding energies of 31.52 and 29.62 eV (Figure 1e), which are attributed to the Ge $3d_{5/2}$ and $3d_{3/2}$ orbitals, respectively. The peaks of Ge $3d_{5/2}$ and $3d_{3/2}$ in the GeH sample possess a higher binding energy in comparison to the pure bulk Ge due to the surface hydrogenation of germanene. The Ge−H bonds were studied by Fourier transform infrared spectroscopy (FT-IR) and solid-state nuclear magnetic resonance spectroscopy (NMR) (Figures S3 and S4). In the FT-IR spectrum, three major peaks at 2000, 800, and ∼500 cm^{-1}, associated with Ge−H vibrations, were observed, which agree well with previous study.[30] The solid-state NMR spectrum of the GeH sample is dominated by a peak at 5.11 ppm of Ge−H bonds, which is consistent with a previous report (Figure S4).[31] It verifies that the dangling bonds in the germanene surface are fully saturated by H atoms.

The temperature dependence of the electrical resistance $R(T)$ of GeH single crystals was measured by using a diamond anvil cell (DAC illustrated in Figure S5) in which the pressure was gradually increased to 34.11 GPa and then released to 5.81 GPa. Electrical resistance was obtained by using an inverting dc current in a van der Pauw technique implemented in a customary cryogenic setup (Figure S6). It is found that a superconducting transition emerges under the compression

https://doi.org/10.1021/jacs.2c05683
J. Am. Chem. Soc. 2022, 144, 18887−18895

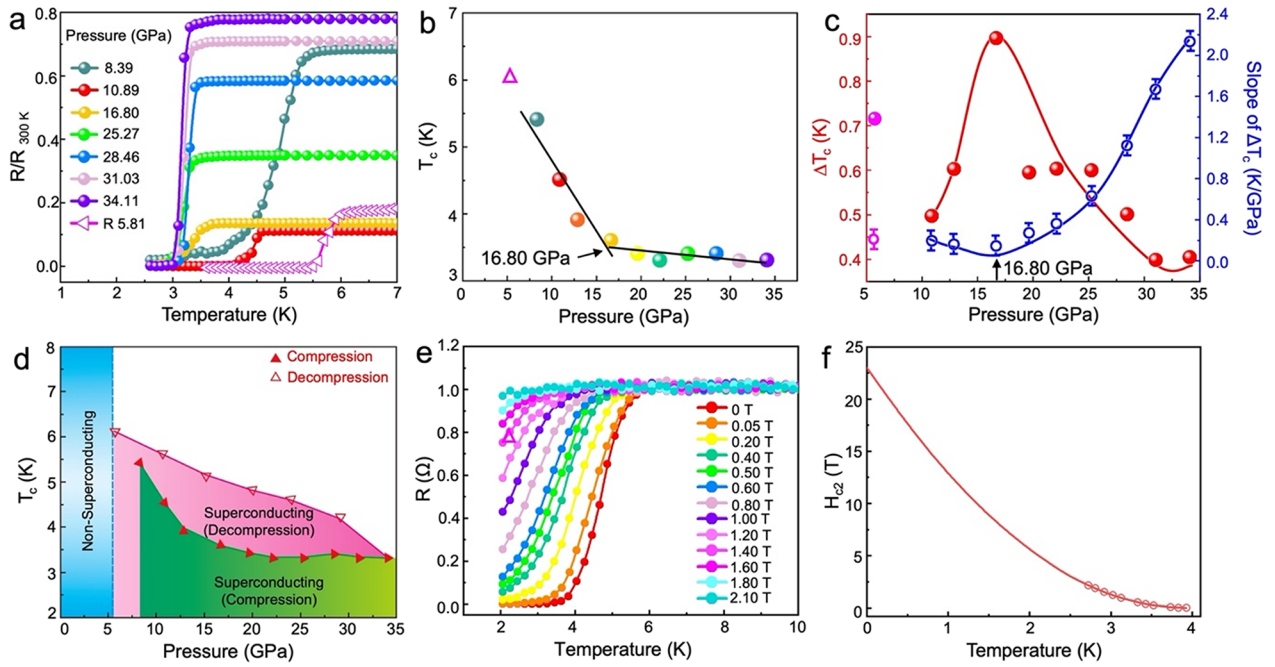

Figure 2. (a) Temperature dependence of the electrical resistance at representative pressures during compression and decompression using a DAC under zero magnetic field. Resistances are normalized by their values at T = 300 K. (b) Superconducting transition temperature as a function of pressure of the GeH sample. (c) The pressure-dependent ΔT_c and the slope of ΔT_c. (d) Temperature−pressure phase diagram of GeH from resistance measurements. The solid and open triangle symbols represent the values of superconducting transition temperature during compression and decompression, respectively. (e) Temperature dependence of the resistance under different magnetic fields up to 2.10 T at 14.62 GPa. (f) Temperature dependence of GeH upper critical field H_{c2}. T_c is defined as the temperature at which resistance drops to 90% of its residual value in the normal state. The red solid line is best fit using the empirical formula $H_{c2}(T) = H_{c2}^* \times [1 - (T/T_c)^2]$ to the experimental data.

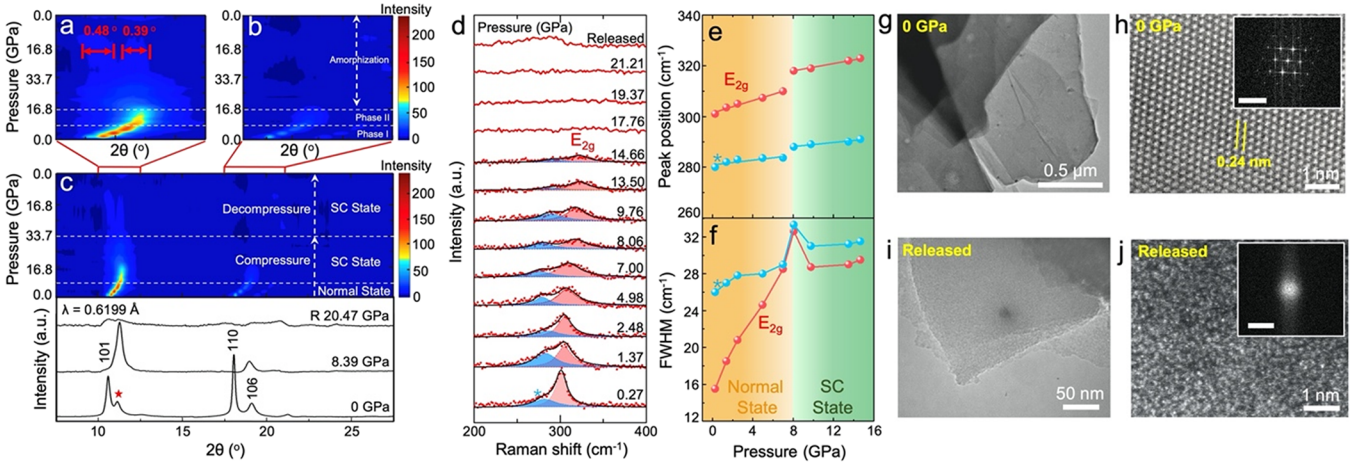

Figure 3. *In situ* high-pressure synchrotron XRD, *in situ* high-pressure Raman spectroscopy and TEM results. (a−c) Intensity contour map of the synchrotron XRD patterns of GeH collected during compression up to 33.71 GPa and decompression to ambient conditions at room temperature (phases identified in a and b). The incident wavelength is λ = 0.6199 Å. (d) Raman spectra of the GeH sample measured at different pressures. All spectra are collected at room temperature. The Raman peaks are fitted with Lorentzian line-shapes. A Raman peak (marked with blue asterisk) has been observed that is attributed to filter cutoff wavelength of the Raman device. (e) Pressure dependence of the Raman peak position for the sample. (f) Pressure dependence of the Raman FWHM for the sample. (g) TEM image of the GeH flake at 0 GPa. (h) HAADF STEM image of GeH at 0 GPa shows its hexagonal lattice with a 2H structure. Inset is the corresponding FFT pattern. Scale bar is 10 1/nm. (i) TEM image of released GeH from 33.71 GPa. (j) HAADF STEM image of GeH released from 30.00 GPa. Inset is the corresponding FFT pattern, which demonstrates the amorphization. Scale bar is 20 1/nm.

pressure of 8.39 GPa, which is demonstrated by a sharp drop of resistance to zero at T_c of 5.41 K (Figure 2a and Figure S7). When the pressure further increases to 34.11 GPa, the superconductivity is retained with a slightly decreased T_c of 3.31 K. Surprisingly, in decompression, the T_c abnormally increases and reaches 6.11 K when the pressure is down to 5.81 GPa. High-pressure magnetoresistance measurement in a magnetic field perpendicular to the *ab* surface of the GeH sample was carried out to obtain further evidence for superconductivity, as shown in Figure 2e. It shows that the T_c is decreased with increased magnetic field, which demonstrates the suppression of superconductivity upon

https://doi.org/10.1021/jacs.2c05683
J. Am. Chem. Soc. 2022, 144, 18887−18895

applied magnetic field. The upper critical magnetic field $H_{c2}(T)$ is estimated to be 23 T at 14.62 GPa according to the equation $H_{c2}(T) = H_{c2}^* \times [1 - (T/T_c)^2]$ (Figure 2f). It is worth noting that $H_{c2}(T)$ at 14.62 GPa is higher than the corresponding Pauli paramagnetic limits (~6.8 T).

To further accurately determine the superconducting transition at high pressure, the T_c and the superconducting transition width (ΔT_c) and slope of ΔT_c*vs* pressure are plotted in Figure 2b,c, respectively. In Figure 2b, the T_c shows two "linearly" decreasing regions of T_c over the entire compression region with a transition point at ~16.80 GPa. Below and above 16.80 GPa, dT_c/dP is determined as −0.216 and −0.012 K/GPa, respectively. This transition point at 16.80 GPa can be also observed in the plotting of the ΔT_c and the slope of ΔT_c*vs* pressure, as shown in Figure 2c. These results indicate that the superconducting behavior of GeH possibly undergoes a second "transition" at 16.80 GPa. We also summarize our experimental results on the pressure dependence of the obtained T_c onset for the studied GeH in Figure 2d. It shows that the superconductivity is gradually suppressed during compression to 34.11 GPa and gradually enhanced during decompression. When the pressure is released down to 5.81 GPa, the highest T_c reaches up to 6.11 K in applied pressure ranges.

To reveal the origin of pressure-induced superconductivity in GeH, *in situ* high-pressure synchrotron XRD and *in situ* high-pressure Raman spectroscopy were carried out, as shown in Figure 3. The structural evolutions of GeH crystal in both compression and decompression processes are plotted in Figure 3a−c (an additional one-dimensional XRD in Figure S8). As the pressure increased from 0 to 16.80 GPa, all diffraction peaks shift linearly to higher angles. Similarly, in the *in situ* high-pressure Raman spectra, the E_{2g} vibrational mode shows a blue shift from 301.0 cm^{-1} at 0.27 GPa to 322.9 cm^{-1} at 14.66 GPa (Figure 3d). At ~8.06 GPa, the peak positions (Figure 3e) and the full width at half-maximum (FWHM) (Figure 3f) values of the Raman peaks exhibit a turning point, indicating a critical pressure point of the superconducting transition.

As shown in Figure 3c, after further compression above 16.80 GPa, a significant broadening of the diffraction peak at 11° is observed. The intensity contour map of the synchrotron XRD patterns shown in Figure 3c implies a gradually shift of the (101) peak of 2H GeH with the successively increased pressure. During the decompression process, the peak is split into two peaks with FWHM of about 0.48° (left) and 0.39° (right), respectively, which is an obvious broadening phenomenon, as illustrated in Figure 3a. Moreover, the E_{2g} peaks disappear at pressure above 16.80 GPa, as shown in Figure 3d. With the pressure released, a soft Raman phonon mode appears between 200 and 300 cm^{-1}, accounting for the enhancement of T_c during the decompression process (Figure 3d). Both XRD and Raman results imply that the interlayer stacking manner of GeH, including interlayer ordering and rotation, may be varied during the compression. In higher pressures, the 2D layered structure with a weak interlayer interaction is possibly collapsed. Thus, it indicates that the pressure-induced amorphization occurs in GeH at pressures above ~16.80 GPa and this amorphous phase remains upon decompression. In addition, the critical pressure (16.80 GPa) in XRD and Raman results coincides to the "knee point" in Figure 2b,c, which suggests that the structural evolution and phase transition play key roles in the superconducting behavior of 2D vdW GeH. As labeled in XRD results in Figure 3, the initial 2H crystal structure of the GeH sample clearly remains up to ~8.39 GPa (phase I) and undergoes a superconducting transition as the pressure rises above ~8.39 GPa (phase II). In further compression with pressure higher than 16.80 GPa, the amorphization occurs and remains in the decompression process.

Pressure-induced amorphization in GeH is also confirmed by the transmission electron microscopy (TEM) and aberration-corrected scanning transmission electron microscopy (STEM) results. Compared with the GeH sample at 0 GPa, GeH released from ~30.00 GPa indeed remains to have a 2D layered structure, but its hexagonal structure has been ruined (Figure 3g−j and Figure S9). As illustrated in Figure 3j, the high-angle annular dark field (HAADF) STEM image of the released GeH shows large-scale disorder with its fast Fourier transform (FFT) diffraction pattern showing diffuse amorphous rings, demonstrating the amorphization at the released GeH sample. These results agree well with *in situ* high-pressure XRD and Raman results. We also carried out an *in situ* low-temperature high-pressure Raman characterization over the GeH sample at 25 K (Figure S10). The results show a similar feature to that of high-pressure Raman spectra measured at room temperature, which reflect that the GeH does not undergo additional phase transition except amorphization under compression during the cooling process.

Compression of 2D vdW materials usually results in uncertain relative interlayer shifting such as slippage and rotation. Meanwhile, the in-plane structure of GeH may also be damaged. However, the results of TEM and STEM show that the samples still possess a 2D layered structure after decompression. From the results of our *in situ* high-pressure Raman spectroscopy, the dehydrogenation process at high pressure has been observed (Figure S10), in which a vibrational mode of H_2 dimers has been identified in a range of 4200 to 4300 cm^{-1} at the pressure greater than 7.7 GPa (the vibrational mode of H_2 at ambient pressure is 4150 cm^{-1}). It verifies the formation of H_2 dimers at high pressure. As indicated by the first principle molecular dynamics result of the GeH (001) surface at 10 GPa, the hydrogen dimer will escape from the material (Figure S11). Alternatively, partial H_2 might escape from the edges, which has been verified by the *in situ* high-pressure synchrotron infrared absorption spectra (Figure S12). The H−Ge−H bending modes disappear with the pressure up to 17.49 GPa. That means that a part of the molecular hydrogen might escape from the edges of GeH sheets, agreeing with the fact that the amorphization transition is an irreversible behavior.

Density functional theory (DFT) calculations were carried out to predict the crystal structure of GeH at high pressures. The calculations of electronic structures, phonon structures, and EPC in GeH under high pressure were also performed. All possible crystal structures and the convex hull diagram of phase stabilities for these predicted Ge_xH_y at 10 GPa are shown in Figure S13. The convex hull is usually used to characterize the stability of high-pressure phases of materials.[32,33] Generally, on the convex hull, the phases are stable and do not decompose into other compounds, while the structures above the convex hull are unstable. Judging by the convex hull of stability, we found that the formation enthalpy of the predicted GeH at 10 GPa using the CALYPSO code is the lowest compared with the other three structures, and it is on the convex hull, while others are not. These results verify that the predicted GeH at

https://doi.org/10.1021/jacs.2c05683
J. Am. Chem. Soc. 2022, 144, 18887−18895

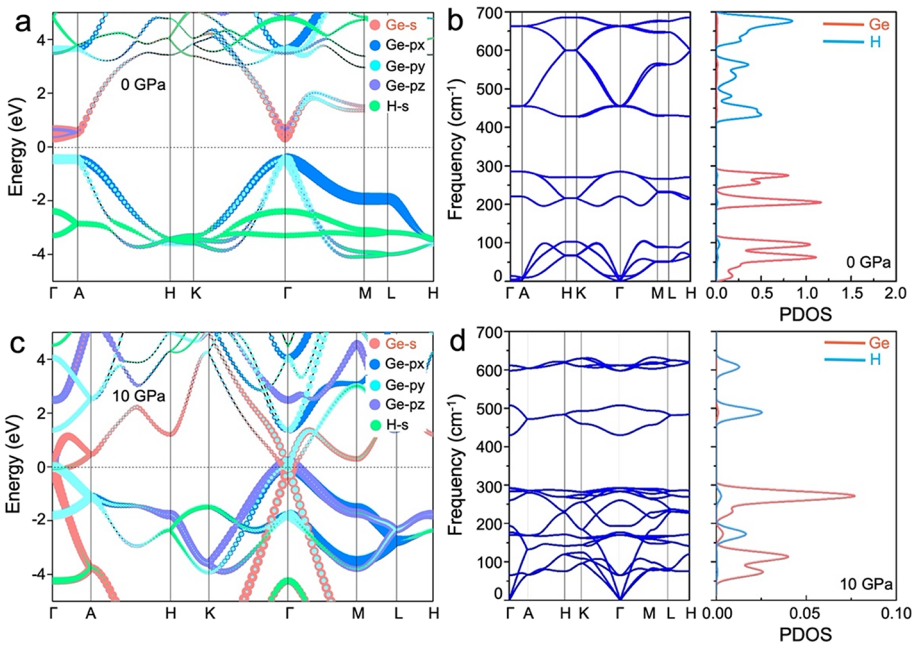

Figure 4. Electronic and phonon structures of 2H GeH. (a) The projected band structure of GeH at 0 GPa. (b) Phonon dispersion and phonon DOS at 0 GPa. (c) The projected band structure of GeH at 10 GPa. (d) Phonon dispersion and phonon DOS at 10 GPa.

10 GPa is the most energy favorable structure. In addition, the metallic feature of the predicted GeH at 10 GPa provides further evidence that the predicted GeH at 10 GPa is the high-pressure superconducting phase in our system (Figure S14). Figure 4a,c shows the electronic structures of GeH at 0 GPa and the predicted GeH at 10 GPa, respectively. At ambient pressure, GeH is a semiconductor with a direct band gap of 0.83 eV, which agrees well with previous studies, as shown in Figure 4a.[22,23] In the high-pressure phase, GeH undergoes a dehydrogenation process with isolated H_2 dimers observed along the *c* axis, which results in the metallic *P*63/*mmc* phase (Figure S13). The band structure of the predicted GeH at 10 GPa in Figure 4c shows that two crossed bands at the Fermi level mainly originating from Ge-*p* and Ge-*s* states play a crucial role in the increased electronic DOS (0.0612 states/eV/unit cell), which is believed to facilitate the superconducting transition. The total DOS and projected DOS of GeH at 0 GPa and predicted GeH at 10 GPa are shown in Figures S15 and S16, respectively, in which H-*s* strongly hybridizes with Ge-p_z at 0 GPa at about −3.2 eV and transforms to slightly hybridize with Ge-p_x and Ge-p_y at 10 GPa at about −2.5 eV, indicating the breaking of the Ge−H bond at high pressures. The energy of H-*s* electrons significantly downshifts from the deep conduction band to the Fermi level, confirming the rising contribution from H atoms in GeH at high pressures. We also performed phonon calculations in the thermodynamic stability range of GeH. As shown in Figure 4b,d, the absence of any imaginary frequency modes in the Brillouin zone (BZ) indicates dynamical stability in both structures. The partial phonon DOS reveals that the heavy Ge atoms dominate the low-frequency modes, while the light H atoms contribute significantly to the high-frequency modes. The appearance of the frequency gap from 100 to 200 cm^{-1} and the disappearance of a frequency gap from 500 to 600 cm^{-1} can be attributed to the formation of H_2 dimers, which will soften the modes of H phonons. The similar structural features to Ge, flat energy bands near the Fermi level, and significant soft phonon modes of GeH at high pressure may relate to its well-established superconducting behavior. The EPC parameter λ, the logarithmic average phonon frequency (ω_{log}), and the Eliashberg phonon spectral function $\alpha^2F(\omega)$[34] have been investigated at 10 GPa. The resulting value of λ is 0.707, which indicates that the EPC effect is fairly strong. It is known that T_c can be estimated from the Allen−Dynes modified McMillan equation: $T_c = \frac{\omega_{log}}{1.2}\exp\left[-\frac{1.04(1+\lambda)}{\lambda - u^*(1+0.62\lambda)}\right]$.[35] In this work, the calculated T_c is 7.7 K by using a typical Coulomb pseudopotential value of $u^* = 0.1$, which is in a good agreement with the experimental results.

Although amorphous hydride superconductivity has been reported, the previous examples all used the hydrogen-induced amorphization method to introduce hydrogen atoms into the crystal to form an alloy,[36,37] such as Pt−Si hydrides. In these hydrides, the introduction of hydrogen generally reduces T_c, and superconductivity is lost when the pressure is released. Moreover, it must involve a hydrogenation or hydrogen absorption process over these alloys at high pressures. It indicates that these alloys are actually *in situ* synthesized at high pressures and then show superconductivity. They do not naturally exist and are not stable at ambient pressure. In contrast, GeH is a stable 2D vdW compound at ambient pressure and demonstrates superconducting transition at high pressures without any *in situ* hydrogenation/absorption process. The superconducting mechanism of compressed GeH is also distinct to 2D FeSe. Unlike superconducting FeSe that retains the pressure-induced T_c via the pressure quenching method at low temperatures,[38] GeH is a semiconductor at 0 GPa and exhibits a pressure-driven semiconducting−superconducting phase transition. Surprisingly, the amorphous GeH sample retains its metallic conduction behavior in the decompression process. The T_c shows an abnormal increase of up to 6.11 K when the pressure is released down to 5.81 GPa rather than showing a reversible

https://doi.org/10.1021/jacs.2c05683
J. Am. Chem. Soc. 2022, 144, 18887−18895

behavior. Alternatively, partial H_2 might escape from the edges, which has been verified by the *in situ* high-pressure synchrotron infrared absorption spectra (Figure S12). The H−Ge−H bending modes disappear at the pressure up to 17.49 GPa. It means that a part of the molecular hydrogen might escape from the edges of GeH sheets, indicating that amorphization transition is an irreversible behavior. The similar behaviors of enhanced superconductivity have also been observed in various systems including elements,[39,40] copper oxides,[41] and various compounds such as CaC_6,[42] In_2Se_3,[43] and P:$BaNi_2As_2$.[44] In the Bardeen−Cooper−Schrieffer (BCS) theory, the EPC parameter λ scale is inversely proportional to the average squared phonon frequency.[45] In our case, the pressure-induced phonon stiffening accounts for the drop of T_c above 16.80 GPa for the amorphous GeH. Conversely, the obverse T_c enhancement in the decompression process is consistent with the Ge−Ge mode softening, further supporting the BCS mechanism of phonon mediated pairing. Enhanced superconductivity caused by a disorder-induced multifractal wavefunction was recently found in monolayer niobium dichalcogenides.[46] The interplay between disorder and superconductivity uncovered here provides a promising platform for a better understanding of the superconducting mechanism.

CONCLUSIONS

In conclusion, pressure-induced superconductivity in 2D vdW GeH is reported, accompanied by a structural phase transition from the 2D crystalline phase to 2D amorphous phase under the pressure of nearly 16.80 GPa. The onset of superconductivity in GeH occurs at 8.39 GPa with a T_c of 5.41 K. The superconductivity arises from the increasing DOS at the Fermi level and the enhanced EPC effect in the compression process, which is confirmed by *in situ* experimental and theoretical results. Superconductivity enhancement is reported in amorphous GeH upon decompression. It is revealed that the evolution of T_c arises from the pressure-induced structural transition and phonon softening related to an in-plane Ge−Ge phonon mode.

MATERIALS AND METHODS

Sample Preparation. In this paper, the hydrogenated germanene (GeH) crystals were prepared using the most popular topochemical deintercalation method, as described in ref 22. In this method, $CaGe_2$ crystals were first synthesized. High purity calcium (Ca) and germanium (Ge) in a stoichiometric ratio of 1:2 were sealed in an evacuated quartz tube. The quartz tube was quickly heated to and held at 1000 °C in a furnace for 25 h and then was cooled down to room temperature. To synthesize the GeH product, the $CaGe_2$ crystals were completely immersed in concentrated HCl acid for a week at −40 °C. This reaction was a displacement process, in which the Ca atoms in $CaGe_2$ were replaced by H atoms in concentrated HCl acid to produce the GeH structure. After the reaction, the GeH was washed with deionized water and anhydrous methanol followed by deionized water to remove contaminants.

Sample Characterization at Ambient Pressure. Powder X-ray diffraction (XRD, PANalytical X9 PertPro X-ray diffractometer using Cu Kα radiation) was performed to study the structure of GeH. The surface morphologies of the GeH samples were investigated using scanning electron microscopy (SEM, JEOL JSM-7500FA). Room-temperature Raman measurements were performed on an inVia Reflex Raman spectrometer with a laser at 532 nm. X-ray photoelectron spectroscopy (XPS) was performed on a Thermo Escalab 250XI photoelectron spectrometer using monochromatic Al Kα radiation under a vacuum at 1×10^{-10} mbar. The details of the crystal structure were further detected by transmission electron microscopy (TEM, JEM-2011F, JEOL operating at 200 kV). High-resolution scanning transmission electron microscopy (STEM) was performed using an FEI Titan Themis Z microscope equipped with probe and image correctors operated at 300 kV. Elemental analysis was performed on an energy dispersive X-ray spectroscopy (EDS, OXFORD INCA X-ACT). Fourier transform infrared (FT-IR) spectrum was collected on a Shimadzu FT-IR Prestige-21 using KBr as the reference sample. The nuclear magnetic resonance spectroscopy (NMR) spectrum was recorded using an AVANCE III HD-600 MHz. The spectrum was taken at a spinning speed of νR = 12.0 kHz, a 2.5 μs excitation pulse, a 10-s relaxation delay, and 32 scans. The experiments were performed at room temperature.

High-Pressure Resistance. Electrical resistance under high pressure was measured by using a four-probe resistance test system in a diamond anvil cell (DAC) at pressures up to 34.11 GPa without a pressure transmitting medium (PTM). Resistance was measured using an inverting dc current in a van der Pauw technique implemented in a customary cryogenic setup (lowest achievable temperature T_{min} = 2.50 K). First, a 250 mm thick metallic gasket of Re was indented with about 17−20 GPa pressure. Then, the bottom of the imprint of diameter about 400 μm was drilled out. An insulating gasket was required to separate the metallic gasket from the electrodes. The Al_2O_3 powder and epoxy mixture was used for the insulating Re gaskets, while gold foil was used in the electrical leads. The diameters of the flat working surface of the diamond anvil and the sample chamber were 400 μm. The samples and a tiny ruby ball beside to calibrate pressure were loaded into the DAC. The resistance values were defined as the average of five successive measurements at a constant temperature. The magnetoelectric measurement is similar to the previous studies.[47,48] The data were collected in a DAC made of nonmagnetic Cu−Be alloy. The diamond culet was 400 μm in diameter. The DAC was placed inside a homemade multifunctional measurement system (1.8−300 K, JANIS Research Company Inc.; 0−9 T, Cryomagnetics Inc.). Helium (He) was used as the medium for heat convection to precisely control the temperature and obtain a high efficiency of heat transfer. Two Cernox resistors (CX-1050-CU-HT-1.4L) located near the DAC were used to ensure the accuracy of the temperature in the presence of a magnetic field.

***In Situ* High-Pressure Synchrotron XRD at Room Temperature.** All high-pressure experiments were carried out by using a symmetric DAC with a 400 μm diameter culet. The GeH sample and a ruby ball were loaded inside a sample chamber, which was laser-drilled to a diameter of 140 μm in a T301 steel gasket that was preindented to a thickness of 50 μm. Silicone oil served as the PTM. High-pressure XRD measurements were carried out at the High-Pressure Station of the Beijing Synchrotron Radiation Facility. The wavelength of the X-ray beam was 0.6199 Å. CeO_2 was used as a standard sample for calibration. The two-dimensional (2D) XRD images were integrated to one-dimensional (1D) patterns with the Dioptas software.

***In Situ* High-Pressure Raman Spectroscopy.** High-pressure Raman at room temperature was performed on a Renishaw inVia Raman Microscope with an Ar^+ 514.5 nm laser, 1800 g/mm grating, and 500 nm blazed wavelength. High pressure was generated by a DAC without PTM. The pressures were determined from the pressure dependent shift of the R1 line fluorescence of ruby. Before high-pressure Raman measurement, the GeH sample was measured from a low intensity of the Raman peak to a high intensity until the sample was damaged. We chose the laser power before damage for high-pressure Raman measurement. In this work, GeH started to get damaged when the power was 1.25 mW; thus, we kept the laser power at 0.80 mW. We have also performed *in situ* high-pressure Raman with silicone oil as PTM at 25 K.

***In Situ* High-Pressure Synchrotron Infrared Spectroscopy.** Infrared spectra experiments were performed using a DAC technique at room temperature. The measurements were carried out at the D-Line IR branch (BL06B) of the Shanghai Synchrotron Radiation Facility (SSRF), Shanghai, China. High pressure was generated by a DAC without PTM. A T301 stainless steel gasket was preindented to

https://doi.org/10.1021/jacs.2c05683
J. Am. Chem. Soc. 2022, 144, 18887−18895

a thickness of 20 μm, and a hole of 140 μm diameter was drilled in the center of the indentation by a laser. The sample and a tiny ruby ball beside to calibrate pressure were loaded into the DAC. The pressures were determined from the pressure dependent shift of the R1 line fluorescence of ruby.

DFT Calculations. A stable crystal structure was predicted for GeH at 10 GPa using the particle-swarm optimization methodology based Crystal Structure Analysis software package with Particle Swarm Optimization (CALYPSO) code.[49,50] Optimization of the electronic structures of GeH was performed using the density functional theory (DFT) within the Perdew−Burke−Ernzerhof parameterization of generalized gradient analysis (GGA), as implemented in the Vienna Ab initio Simulation Package (VASP) code.[51] The projector augmented wave (PAW) method was employed to describe electron−ion interactions.[52] Brillouin zone (BZ) sampling used a grid with a spacing of 15 × 15 × 11 and a plane-wave basis cutoff set at 500 eV. Equilibrium geometries were obtained by the minimum energy principle until the energy and force converged to 10^{-6} eV and 10^{-4} eV/Å, respectively. Phonon dispersion curves and normal modes were obtained by applying the supercell method in PHONOPY code.[53] Lattice dynamics and electron−phonon coupling (EPC) calculations of GeH at 10 GPa were performed with the QUANTUM-ESPRESSO package[54] using Optimized Norm-Conserving Vanderbilt (ONCV) pseudopotentials[55] and plane wave basis sets with a kinetic energy cutoff of 180 Ry. A 24 × 24 × 24 Monkhorst−Pack k-point grid with a Gaussian smearing of 0.01 Ry and a 2 × 2 × 2 q-point mesh in the first BZ was used for the calculation of EPC matrix elements.

■ ASSOCIATED CONTENT

Supporting Information

The Supporting Information is available free of charge at https://pubs.acs.org/doi/10.1021/jacs.2c05683.

Additional experimental data and calculation results including XRD pattern of GeH powder, SEM, EDS, FT-IR, solid-state NMR, schematic illustration of the DAC, schematics of the sample chamber configuration, temperature dependence of the electrical resistance at representative pressures, structural properties of GeH under high pressures, TEM, *in situ* high-pressure Raman spectra, *in situ* high-pressure synchrotron infrared absorption spectra, first principle molecular dynamics result of GeH (001) surface at 10 GPa, the possible structures of GeH under high pressure, phase stabilities, band structure of predicted GeH at 10 GPa, total DOS, and projected DOS at different pressures (PDF)

■ AUTHOR INFORMATION

Corresponding Authors

Quanjun Li − *State Key Laboratory of Superhard Materials, Jilin University, Changchun 130012, China;* orcid.org/0000-0002-4718-4156; Email: liquanjun@jlu.edu.cn

Bingbing Liu − *State Key Laboratory of Superhard Materials, Jilin University, Changchun 130012, China;* orcid.org/0000-0003-3989-0891; Email: liubb@jlu.edu.cn

Yi Du − *School of Physics and Centre of Quantum and Matter Sciences, International Research Institute for Multidisciplinary Science, Beihang University, Beijing 100191, China; BUAA-UOW Joint Research Centre, Institute for Superconducting and Electronic Materials (ISEM), Australian Institute for Innovative Materials (AIIM), University of Wollongong, Wollongong, New South Wales 2500, Australia;* orcid.org/0000-0003-1932-6732; Email: yi_du@buaa.edu.cn

Authors

Yilian Xi − *School of Physics and Centre of Quantum and Matter Sciences, International Research Institute for Multidisciplinary Science, Beihang University, Beijing 100191, China; BUAA-UOW Joint Research Centre, Institute for Superconducting and Electronic Materials (ISEM), Australian Institute for Innovative Materials (AIIM), University of Wollongong, Wollongong, New South Wales 2500, Australia*

Xiaoling Jing − *State Key Laboratory of Superhard Materials, Jilin University, Changchun 130012, China*

Zhongfei Xu − *School of Physics, Beihang University, Beijing 100191, China; BUAA-UOW Joint Research Centre, Institute for Superconducting and Electronic Materials (ISEM), Australian Institute for Innovative Materials (AIIM), University of Wollongong, Wollongong, New South Wales 2500, Australia; College of Environmental Science and Engineering, North China Electric Power University, Beijing 102206, China*

Nana Liu − *School of Physics, Beihang University, Beijing 100191, China; BUAA-UOW Joint Research Centre, Institute for Superconducting and Electronic Materials (ISEM), Australian Institute for Innovative Materials (AIIM), University of Wollongong, Wollongong, New South Wales 2500, Australia*

Yani Liu − *School of Physics, Beihang University, Beijing 100191, China; BUAA-UOW Joint Research Centre, Institute for Superconducting and Electronic Materials (ISEM), Australian Institute for Innovative Materials (AIIM), University of Wollongong, Wollongong, New South Wales 2500, Australia*

Miao-Ling Lin − *State Key Laboratory of Superlattices and Microstructures, Institute of Semiconductors, Chinese Academy of Sciences, Beijing 100083, China;* orcid.org/0000-0001-5838-8237

Ming Yang − *School of Physics, Beihang University, Beijing 100191, China*

Ying Sun − *School of Physics, Beihang University, Beijing 100191, China;* orcid.org/0000-0003-0590-372X

Jincheng Zhuang − *School of Physics, Beihang University, Beijing 100191, China; BUAA-UOW Joint Research Centre, Institute for Superconducting and Electronic Materials (ISEM), Australian Institute for Innovative Materials (AIIM), University of Wollongong, Wollongong, New South Wales 2500, Australia;* orcid.org/0000-0003-3632-1108

Xun Xu − *School of Physics, Beihang University, Beijing 100191, China; BUAA-UOW Joint Research Centre, Institute for Superconducting and Electronic Materials (ISEM), Australian Institute for Innovative Materials (AIIM), University of Wollongong, Wollongong, New South Wales 2500, Australia;* orcid.org/0000-0002-0504-362X

Weichang Hao − *School of Physics and Centre of Quantum and Matter Sciences, International Research Institute for Multidisciplinary Science, Beihang University, Beijing 100191, China; BUAA-UOW Joint Research Centre, Institute for Superconducting and Electronic Materials (ISEM), Australian Institute for Innovative Materials (AIIM), University of Wollongong, Wollongong, New South Wales 2500, Australia;* orcid.org/0000-0002-1597-7151

Yanchun Li − *Beijing Synchrotron Radiation Facility, Institute of High Energy Physics, Chinese Academy of Sciences, Beijing 100049, China*

Xiaodong Li − *Beijing Synchrotron Radiation Facility, Institute of High Energy Physics, Chinese Academy of Sciences, Beijing 100049, China;* orcid.org/0000-0002-2290-1198

Xiangjun Wei − *Shanghai Synchrotron Radiation Facility (SSRF), Shanghai Advanced Research Institute, Chinese Academy of Sciences, Shanghai 201204, China*

Ping-Heng Tan − *State Key Laboratory of Superlattices and Microstructures, Institute of Semiconductors, Chinese Academy of Sciences, Beijing 100083, China;* orcid.org/0000-0001-6575-1516

Shi Xue Dou − *School of Physics and Centre of Quantum and Matter Sciences, International Research Institute for Multidisciplinary Science, Beihang University, Beijing 100191, China; BUAA-UOW Joint Research Centre, Institute for Superconducting and Electronic Materials (ISEM), Australian Institute for Innovative Materials (AIIM), University of Wollongong, Wollongong, New South Wales 2500, Australia;* orcid.org/0000-0003-3824-7693

Complete contact information is available at: https://pubs.acs.org/10.1021/jacs.2c05683

Author Contributions

◆Y.X., X.J., and Z.X. contributed equally to this work.

Notes

The authors declare no competing financial interest.

■ ACKNOWLEDGMENTS

This work was financially supported by the National Key R&D Program of China (2018YFE0202700 and 2018YFA0305900), Beijing Natural Science Foundation (Z180007), Australian Research Council (DP170101467, FT180100585, and LP180100722), National Natural Science Foundation of China (52073006, 51672018, 51472016, 11874003, 11874172, U2032215, 11904015, 12074021, and 51320105007), and the Fundamental Research Funds for the Central Universities (YWF-22-K-101). The authors acknowledge the support from the UOW-BUAA Joint Research Centre. The authors thank the D-Line IR branch (BL06B) of the Shanghai Synchrotron Radiation Facility (SSRF) for use of the synchrotron radiation facilities. The authors thank Dr. H.F. Feng for proofreading and valuable discussion.

■ REFERENCES

(1) Tsen, A. W.; Hunt, B.; Kim, Y. D.; Yuan, Z. J.; Jia, S.; Cava, R. J.; Hone, J.; Kim, P.; Dean, C. R.; Pasupathy, A. N. Nature of the quantum metal in a two-dimensional crystalline superconductor. *Nat. Phys.* **2016**, *12*, 208−212.

(2) Saito, Y.; Nojima, T.; Iwasa, Y. Highly crystalline 2D superconductors. *Nat. Rev. Mater.* **2017**, *2*, 16094.

(3) Liao, M.; Zang, Y.; Guan, Z.; Li, H.; Gong, Y.; Zhu, K.; Hu, X.-P.; Zhang, D.; Xu, Y.; Wang, Y.-Y.; He, K.; Ma, X.-C.; Zhang, S.-C.; Xue, Q.-K. Superconductivity in few-layer stanene. *Nat. Phys.* **2018**, *14*, 344−348.

(4) Fatemi, V.; Wu, S.; Cao, Y.; Bretheau, L.; Gibson, Q. D.; Watanabe, K.; Taniguchi, K.; Cava, R. J.; Jarillo-Herrero, P. Electrically tunable low-density superconductivity in a monolayer topological insulator. *Science* **2018**, *362*, 926−929.

(5) Profeta, G.; Calandra, M.; Mauri, F. Phonon-mediated superconductivity in graphene by lithium deposition. *Nat. Phys.* **2012**, *8*, 131−134.

(6) Kim, J. S.; Kremer, R. K.; Boeri, L.; Razavi, F. S. Specific heat of the Ca-intercalated graphite superconductor CaC_6. *Phys. Rev. Lett.* **2006**, *96*, No. 217002.

(7) Weller, T. E.; Ellerby, M.; Saxena, S. S.; Smith, R. P.; Skipper, N. T. Superconductivity in the intercalated graphite compounds C_6Yb and C_6Ca. *Nat. Phys.* **2005**, *1*, 39−41.

(8) Ichinokura, S.; Sugawara, K.; Takayama, A.; Takahashi, T.; Hasegawa, S. Superconducting calcium-intercalated bilayer graphene. *ACS Nano* **2016**, *10*, 2761−2765.

(9) Emery, N.; Hérold, C.; d'Astuto, M.; Garcia, V.; Bellin, C.; Marêché, J. F.; Lagrange, P.; Loupias, G. Superconductivity of bulk CaC_6. *Phys. Rev. Lett.* **2005**, *95*, No. 087003.

(10) Cao, Y.; Fatemi, V.; Fang, S.; Watanabe, K.; Taniguchi, T.; Kaxiras, E.; Jarillo-Herrero, P. Unconventional superconductivity in magic-angle graphene superlattices. *Nature* **2018**, *556*, 43−50.

(11) Molle, A.; Goldberger, J.; Houssa, M.; Xu, Y.; Zhang, S. C.; Akinwande, D. Buckled two-dimensional Xene sheets. *Nat. Mater.* **2017**, *16*, 163−169.

(12) Li, L.; Lu, S. Z.; Pan, J.; Qin, Z.; Wang, Y.; Wang, Y.; Cao, G. Y.; Du, S.; Gao, H. J. Buckled germanene formation on Pt (111). *Adv. Mater.* **2014**, *26*, 4820−4824.

(13) Derivaz, M.; Dentel, D.; Stephan, R.; Hanf, M. C.; Mehdaoui, A.; Sonnet, P.; Pirri, C. Continuous germanene layer on Al (111). *Nano Lett.* **2015**, *15*, 2510−2516.

(14) Liu, C. C.; Feng, W.; Yao, Y. Quantum spin Hall effect in silicene and two-dimensional germanium. *Phys. Rev. Lett.* **2011**, *107*, No. 076802.

(15) Zhuang, J.; Gao, N.; Li, Z.; Xu, X.; Wang, J.; Zhao, J.; Dou, S. X.; Du, Y. Cooperative electron−phonon coupling and buckled structure in germanene on Au (111). *ACS Nano* **2017**, *11*, 3553−3559.

(16) Acun, A.; Zhang, L.; Bampoulis, P.; Farmanbar, M.; van Houselt, A.; Rudenko, A. N.; Lingenfelder, M.; Brocks, G.; Poelsema, B.; Katsnelson, M. I.; Zandvliet, H. J. W. Germanene: the germanium analogue of graphene. *J. Phys. Condens. Matter.* **2015**, *27*, No. 443002.

(17) Zhuang, J. C.; Liu, C.; Zhou, Z. Y.; Casillas, G.; Feng, H. F.; Xu, X.; Wang, J. O.; Hao, W. C.; Wang, X. L.; Dou, S. X.; Hu, Z. P.; Du, Y. Dirac signature in germanene on semiconducting substrate. *Adv. Sci.* **2018**, *5*, 1800207.

(18) Liu, Y.; Zhuang, J.; Hao, W.; Du, Y. Raman studies on silicene and germanene. *Surf. Innov.* **2017**, *6*, 4−12.

(19) Zhang, L.; Bampoulis, P.; Rudenko, A. N.; Yao, Q. V.; Van Houselt, A.; Poelsema, B.; Katsnelson, M. I.; Zandvliet, H. J. W. Structural and electronic properties of germanene on MoS_2. *Phys. Rev. Lett.* **2016**, *116*, No. 256804.

(20) Amlaki, T.; Bokdam, M.; Kelly, P. J. Z_2 invariance of germanene on MoS_2 from first principles. *Phys. Rev. Lett.* **2016**, *116*, No. 256805.

(21) Cahangirov, S.; Topsakal, M.; Aktürk, E.; Şahin, H.; Ciraci, S. Two- and one-dimensional honeycomb structures of silicon and germanium. *Phys. Rev. Lett.* **2009**, *102*, No. 236804.

(22) Bianco, E.; Butler, S.; Jiang, S.; Restrepo, O. D.; Windl, W.; Goldberger, J. E. Stability and exfoliation of germanane: a germanium graphane analogue. *ACS Nano* **2013**, *7*, 4414−4421.

(23) Cultrara, N. D.; Wang, Y.; Arguilla, M. Q.; Scudder, M. R.; Jiang, S.; Windl, W.; Bobev, S.; Goldberger, J. E. Synthesis of 1T, 2H, and 6R germanane polytypes. *Chem. Mater.* **2018**, *30*, 1335−1343.

(24) Serino, A. C.; Ko, J. S.; Yeung, M. T.; Schwartz, J. J.; Kang, C. B.; Tolbert, S. H.; Kaner, R. B.; Dunn, B. S.; Weiss, P. S. Lithium-ion insertion properties of solution-exfoliated germanane. *ACS Nano* **2017**, *11*, 7995−8001.

(25) Jiang, S.; Bianco, J.; Goldberger, J. E. The structure and amorphization of germanane. *J. Mater. Chem. C* **2014**, *2*, 3185−3188.

(26) Yao, Q.; Zhang, L.; Kabanov, N. S.; Rudenko, A. N.; Arjmand, T.; Rahimpour Soleimani, H.; Klavsyuk, A. L.; Zandvliet, H. J. W. Bandgap opening in hydrogenated germanene. *Appl. Phys. Lett.* **2018**, *112*, 171607.

(27) Chen, Q.; Liang, L.; Potsi, G.; Wan, P.; Lu, J.; Giousis, T.; Thomou, E.; Gournis, D.; Rudolf, P.; Ye, J. Highly conductive metallic state and strong spin−orbit interaction in annealed germanane. *Nano Lett.* **2019**, *19*, 1520−1526.

(28) Madhushankar, B. N.; Kaverzin, A.; Giousis, T.; Potsi, G.; Gournis, D.; Rudolf, P.; Blake, G. R.; Van Der Wal, C. H.; Van Wees,

B. J. Electronic properties of germanane field-effect transistors. *2D Mater.* **2017**, *4*, No. 021009.
(29) Liu, N.; Qiao, H.; Xu, K.; Xi, Y.; Ren, L.; Cheng, N.; Cui, D.; Qi, X.; Xu, X.; Hao, W.; Dou, S. X.; Du, Y. Hydrogen Terminated Germanene for a Robust Self-Powered Flexible Photoelectrochemical Photodetector. *Small* **2020**, *16*, 2000283.
(30) Ng, S.; Sturala, J.; Vyskocil, J.; Lazar, P.; Martincova, J.; Plutnar, J.; Pumera, M. Two-Dimensional Functionalized Germananes as Photoelectrocatalysts. *ACS Nano* **2021**, *15*, 11681−11693.
(31) Giousis, T.; Potsi, G.; Kouloumpis, A.; Spyrou, K.; Georgantas, Y.; Chalmpes, N.; Dimos, K.; Antoniou, M. K.; Papavassiliou, G.; Bourlinos, A. B.; Kim, H. J.; Wadi, V. K. S.; Alhassan, S.; Ahmadi, M.; Kooi, B. J.; Blake, G.; Balazs, D. M.; Loi, M. A.; Gournis, D.; Rudolf, P. Synthesis of 2D Germanane (GeH): a New, Fast, and Facile Approach. *Angew. Chem., Int. Ed.* **2021**, *60*, 360−365.
(32) Li, X.; Peng, F. Superconductivity of pressure-stabilized vanadium hydrides. *Inorg. Chem.* **2017**, *56*, 13759−13765.
(33) Zhu, Q.; Oganov, A. R.; Lyakhov, A. O. Novel stable compounds in the Mg−O system under high pressure. *Phys. Chem. Chem. Phys.* **2013**, *15*, 7696−7700.
(34) Allen, P. B. Neutron spectroscopy of superconductors. *Phys. Rev. B* **1972**, *6*, 2577−2579.
(35) Allen, P. B.; Dynes, R. C. Transition temperature of strong-coupled superconductors reanalyzed. *Phys. Rev. B* **1975**, *12*, 905−922.
(36) Yeh, X. L.; Samwer, K.; Johnson, W. L. Formation of an amorphous metallic hydride by reaction of hydrogen with crystalline intermetallic compounds-a new method of synthesizing metallic glasses. *Appl. Phys. Lett.* **1983**, *42*, 242−243.
(37) Traverse, A.; Bernas, H.; Chaumont, J.; Fan, X. J.; Mendoza-Zelis, L. Resistive and superconducting properties of the amorphous Pd-Si hydride. *Phys. Rev. B* **1984**, *30*, 6413−6418.
(38) Deng, L.; Bontke, T.; Dahal, R.; Xie, Y.; Gao, B.; Li, X.; Yin, K.; Gooch, M.; Rolston, D.; Chen, T.; Wu, Z.; Ma, Y.; Dai, P.; Chu, C. Pressure-induced high-temperature superconductivity retained without pressure in FeSe single crystals. *Proc. Natl. Acad. Sci.* **2021**, *118*, No. e2108938118.
(39) Mauri, F.; Zakharov, O.; de Gironcoli, S.; Louie, S. G.; Cohen, M. L. Phonon softening and superconductivity in tellurium under pressure. *Phys. Rev. Lett.* **1996**, *77*, 1151−1154.
(40) Profeta, G.; Franchini, C.; Lathiotakis, N. N.; Floris, A.; Sanna, A.; Marques, M. A. L.; Lüders, M.; Massidda, S.; Gross, E. K. U.; Continenza, A. Superconductivity in lithium, potassium, and aluminum under extreme pressure: A first-principles study. *Phys. Rev. Lett.* **2006**, *96*, No. 047003.
(41) Reznik, D.; Pintschovius, L.; Ito, M.; Iikubo, S.; Sato, M.; Goka, H.; Fujita, M.; Yamada, K.; Gu, G. D.; Tranquada, J. M. Electron−phonon coupling reflecting dynamic charge inhomogeneity in copper oxide superconductors. *Nature* **2006**, *440*, 1170−1173.
(42) Gauzzi, A.; Takashima, S.; Takeshita, N.; Terakura, C.; Takagi, H.; Emery, N.; Hérold, C.; Lagrange, P.; Loupias, G. Enhancement of superconductivity and evidence of structural instability in intercalated graphite CaC_6 under high pressure. *Phys. Rev. Lett.* **2007**, *98*, No. 067002.
(43) Ke, F.; Dong, H.; Chen, Y.; Zhang, J.; Liu, C.; Zhang, J.; Gan, Y.; Han, Y.; Chen, Z.; Gao, C.; Wen, J.; Yang, W.; Chen, X. J.; Struzhkin, V. V.; Mao, H. K.; Chen, B. Decompression-Driven Superconductivity Enhancement in In_2Se_3. *Adv. Mater.* **2017**, *29*, 1701983.
(44) Kudo, K.; Takasuga, M.; Okamoto, Y.; Hiroi, Z.; Nohara, M. Giant phonon softening and enhancement of superconductivity by phosphorus doping of $BaNi_2As_2$. *Phys. Rev. Lett.* **2012**, *109*, No. 097002.
(45) Allen, P. B.; Cohen, M. L. Superconductivity and phonon softening. *Phys. Rev. Lett.* **1972**, *29*, 1593−1596.
(46) Zhao, K.; Lin, H.; Xiao, X.; Huang, W.; Yao, W.; Yan, M.; Xing, Y.; Zhang, Q.; Li, Z. X.; Hoshino, S.; Wang, J.; Zhou, S.; Gu, L.; Bahramy, M. S.; Yao, H.; Nagaosa, N.; Xue, Q. K.; Law, K. T.; Chen, X.; Ji, S. H. Disorder-induced multifractal superconductivity in monolayer niobium dichalcogenides. *Nat. Phys.* **2019**, *15*, 904−910.
(47) Zhou, Y.; Wu, J.; Ning, W.; Li, N.; Du, Y.; Chen, X.; Zhang, R.; Chi, Z.; Wang, X.; Zhu, X.; Lu, P. Pressure-induced superconductivity in a three-dimensional topological material $ZrTe_5$. *Proc. Natl. Acad. Sci.* **2016**, *113*, 2904−2909.
(48) Snider, E.; Dasenbrock-Gammon, N.; McBride, R.; Debessai, M.; Vindana, H.; Vencatasamy, K.; Lawler, K. V.; Salamat, A.; Dias, R. P. Room-temperature superconductivity in a carbonaceous sulfur hydride. *Nature* **2020**, *586*, 373−377.
(49) Wang, Y.; Lv, J.; Zhu, L.; Ma, Y. CALYPSO: A method for crystal structure prediction. *Comput. Phys. Commun.* **2012**, *183*, 2063−2070.
(50) Wang, Y.; Lv, J.; Zhu, L.; Ma, Y. Crystal structure prediction via particle-swarm optimization. *Phys. Rev. B* **2010**, *82*, No. 094116.
(51) Blöchl, P. E. Projector augmented-wave method. *Phys. Rev. B* **1994**, *50*, 17953−17979.
(52) Perdew, J. P.; Burke, K.; Ernzerhof, M. Generalized gradient approximation made simple. *Phys. Rev. Lett.* **1996**, *77*, 3865−3868.
(53) Togo, A.; Oba, F.; Tanaka, I. First-principles calculations of the ferroelastic transition between rutile-type and $CaCl_2$-type SiO_2 at high pressures. *Phys. Rev. B* **2008**, *78*, No. 134106.
(54) Giannozzi, P.; Baroni, S.; Bonini, N.; Calandra, M.; Car, R.; Cavazzoni, C.; Ceresoli, D.; Chiarotti, G. L.; Cococcioni, M.; Dabo, I.; Dal Corso, A.; de Gironcoli, S.; Fabris, S.; Fratesi, G.; Gebauer, R.; Gerstmann, U.; Gougoussis, C.; Kokalj, A.; Lazzeri, M.; Martin-Samos, L.; Marzari, N.; Mauri, F.; Mazzarello, R.; Paolini, S.; Pasquarello, A.; Paulatto, L.; Sbraccia1, C.; Scandolo, S.; Sclauzero, G.; Seitsonen, A. P.; Smogunov, A.; Umari, P.; Wentzcovitch, R. M. QUANTUM ESPRESSO: a modular and open-source software project for quantum simulations of materials. *J. Phys. Condens. Matter.* **2009**, *21*, No. 395502.
(55) Hamann, D. R. Optimized norm-conserving Vanderbilt pseudopotentials. *Phys. Rev. B* **2013**, *88*, No. 085117.